Computer Methods in Applied Mechanics and Engineering 431 (2024) 117239

Contents lists available at ScienceDirect

Computer Methods in Applied Mechanics and Engineering

journal homepage: www.elsevier.com/locate/cma

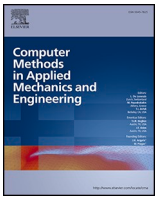

A novel neural-network non-ordinary state-based peridynamic method for large deformation and fracture analysis of hyperelastic membrane

Yang Yang [a,*], Yujie Chen [b], Yijun Liu [b]

[a] Faculty of Material Science, Shenzhen MSU-BIT University, Shenzhen, Guangdong, 518172, China
[b] Department of Mechanics and Aerospace Engineering, Southern University of Science and Technology, Shenzhen, China

HIGHLIGHTS

- A novel neural network non-ordinary state-based peridynamic (NOSB PD) algorithm is developed.
- This approach can successfully overcome the zero-energy problem and significantly improves the efficiency.
- A non-local membrane theory has been developed by approximating the curved horizon of the membrane as a flat surface and applying the plane stress assumption locally.
- Deformation gradients are represented by their corresponding bond vectors based on the non-local geometry relationship.
- Nonlinear bijection between bond vectors and force density is obtained using neural networks.
- Modeling of large deformation, out of plane tearing, wrinkle as well as fracture of hyperelastic membranes can be achieved.

ARTICLE INFO

Keywords:
Neural networks
Non-ordinary peridynamics
Hyperelastic membrane
Large deformation
Fracture

ABSTRACT

This paper presents a novel neural network non-ordinary state-based peridynamic (NOSB PD) algorithm for large deformation and fracture analysis of hyperelastic membranes. A non-local membrane theory has been developed by approximating the curved horizon of the membrane as a flat surface and applying the plane stress assumption locally. This allows the simulation of the membrane structure using a single layer of material points, simplifying implementation, improving efficiency, and avoiding volume locking. In the framework of NOSB PD, the deformation gradients are represented by their corresponding bond vectors based on the non-local geometry relationship. Then, the nonlinear bijection between bond vectors and force density is obtained using a developed neural network model. This approach successfully overcomes the zero-energy problem and significantly improves the efficiency. Three representative numerical examples: out of plane deformation, out of plane loading crack propagation and penetrating of a ball are simulated to validate the developed algorithm. The results demonstrate that the developed method can accurately and efficiently achieve the large deformation, out of plane tearing, wrinkle as well as fracture of hyperelastic membranes.

* Corresponding author.
E-mail address: yangy2023@smbu.edu.cn (Y. Yang).

https://doi.org/10.1016/j.cma.2024.117239
Received 24 April 2024; Received in revised form 23 June 2024; Accepted 14 July 2024
Available online 30 July 2024

1. Introduction

Membranes are special structures created based on the sprite of natural shapes, such as the skeleton of animals and the leaves of plants. Membranes are lightweight and can withstand tensile loads, whereas they wrinkle when a small compressive or shear load is applied. These have been extensively used as foldable components in aerospace engineering. In recent years, hyperelastic materials have become an area of extensive research due to their superior characteristics [1,2], which are essential for improving the development of biomedicine [3] and soft devices [4]. As a result, the hyperelastic membranes have become essential components in various applications. Because of their unique features, it is crucial to thoroughly understand the deformation and actuating mechanisms of hyperelastic membranes for their practical engineering applications.

Modeling large deformation and failure of materials and structures is still a challenging task in computational mechanics. This is because large deformation can cause a distortion of discretized meshes, which makes convergence difficult. Based on spatial derivative, the classical continuum mechanics faces inherent difficulties in describing spatial discontinuity and singular stress filed around a crack. However, the peridynamic (PD) theory [5] provides a particle discretized model that describes the material and structure response in a non-local integral description. This relaxation of the requirement for the continuity of the displacement field. The failure initiation and propagation can be captured and represented naturally and spontaneously without extra artificial treatment.

Within the realm of PD, the interaction between two material points is responded by a bond force that is similar to a spring force. The calculation of this bond force depends on the extent to the bond has stretched, which can be linked to the concept of strain in classical continue mechanics. Fracture occurs when the bond stretch exceeds the critical stretch value, which indicates the energy release rate of the material property in the context of fracture mechanics. PD has been proven to be a valuable tool for the simulation of large deformation and fracture-related concerns [6,7,8].

Silling and Bobaru [9] used a bond-based PD model to approximate the large deformation and failure behavior of rubber membranes. This method employs a constitutive model of rubber material under a particular loading condition. However, due to the lack of bonds extending to particles off the surface, a given force density will result in different bulk material responses using the governing equation based on 3D expression. Bang and Madenci [10] presented the PD modeling of hyperelastic membrane deformation using the Neo-Hookean model to simulate material behavior. Equibiaxial, planar and uniaxial loading conditions were considered in the analyses. The material parameters for each loading case were determined by equating the PD strain energy density to that of the classical continuum mechanics. The results were compared well with finite element analysis. Li et al. [11] studied the quasi-static behaviors of membranes with an implicit bond-based PD computational framework. They developed a bimodular material model in PD, which was extended to deal with the wrinkling and fracture problems of membranes by setting the compressive micro-modulus to zero. Yin et al. [12] formulated the nonlinear bond force according to the expression of the principal stress of hyperelastic models. Most of the work mentioned above relies on the bond-based PD model. However, BB PD has a significant drawback: Poisson's ratio is fixed at 1/3 for plane stress, and 1/4 for plain strain and 3D problems [13]. With some modifications, BB PD can involve plasticity and rate-dependent behaviors [14,15,16]. It can also capture the large deformation of the hyperelastic under particular loading conditions. However, these BB models are based on special loading conditions and may fail to predict the mechanical response in complex deformation.

In 2007, non-ordinary state-based peridynamics (NOSB-PD), which has been developed by Silling [17,18]. NOSB-PD connects the concept of stress and strain via the deformation gradient tensor, so that the constitutive relations in traditional continuum mechanics can be directly used. Behera et al. and Roy et al. [19] developed PD correspondence models for Neo-Hookean material as well as Anand and Talamini-Mao-Anand models [20], respectively. Ozdemir et al. [21] developed a viscoelastic material model in the ordinary state-based PD framework to capture crack propagation in polymeric water treatment membranes. Chen et al. [22,23] utilized the NOSB-PD to analyze the large deformation, crack propagation, and fatigue of hydrogel. However, conventional NOSB PD suffers from zero-energy modes, which can cause significant numerical oscillation due to a non-unique mapping between the deformation states and force states. To control the nonphysical oscillations and improve numerical results, many stabilization techniques have been developed, such as introducing a fictitious spring force to a bond [18], using the average displacement correction over a horizon [17] and applying higher-order deformation gradient tensor [24]. One of the most promising solutions to zero-energy modes is bond-associated (BA) non-ordinary state-based (NOSB) PD [25]. In this scheme, the deformation gradient of a bond is formed in the intersection region of the two endpoints, avoiding the zero-energy mode inherently without extra corrections or affecting the material characteristics [25,26,27]. Based on BA NOSB PD, Behera et al. [19] and Roy et al. [20] analyzed the finite elastic deformation and rupture in Neo-Hookean materials as well as polymers predicted by Anand and Talamini-Mao-Anand (TMA) models, respectively. The numerical results are in good agreement with the experimental data. Chen et al. studied the fracture and fatigue behaviors of hydrogel [22,23].

As a non-local theory, the PD method is more computationally costly than the local method. This is because more long-range forces are considered in the PD model. In bond-associated scheme, calculating the deformation gradient of each bond instead of each point leads to a relatively high computational expense. Although PD can be coupled with finite element method [28,29] and boundary element method [30,31] to reduce the computational cost, a high-performance algorithm for large deformation, wrinkle simulation and fracture analysis of hyperelastic membranes is also of importance. Data-driven techniques have become a invaluable for helping computational mechanics solve challenging problems. The use of a data-driven approach to obtain force-field has been extensively used in molecular dynamics [32,33] and PD [34,35], and the same idea will be utilized in this study.

In this article, a novel method is pursued using the neural network in the framework of NOSB PD for hyperelastic membrane analysis. A non-local membrane theory has been developed by approximating the curving horizon of the membrane as a flat surface and applying the plane stress assumption locally. Gent model has been employed to simulate the constitutive of hyperelastic material. Using bond vectors to specify the non-local deformation gradient, and establish a neural network model to construct the nonlinear

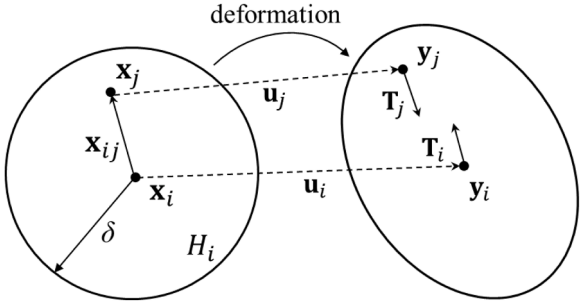

Fig. 1. Peridynamic diagram and notations.

mapping relationship between bond vectors and force states. The proposed algorithm is free of the zero-energy modes and significantly improves the efficiency.

This paper is organized as follows. A brief review of the NOSB PD formulation is presented in Section 2. A membrane theory is derived in Section 3. In Section 4, the PD constitutive model and the proposed NN NOSB PD method are elaborated. Section 5 shows the training data preparation and the framework of the NN model applied in the membrane model. Numerical examples are presented in Section 6.

2. Non-ordinary state-based peridynamic theory

The NOSB PD theory is proposed in Ref. [17]. As shown in Fig. 1, the considered domain is discretized by the material points. A material point with index i has the initial position vector x_i. According to nonlocal theory, each material point can interact with other material points within the horizon H_i. H_i is usually characterized by a circle centered at i with radius of δ. The material points within the horizon are referred to as neighborhood points of the center point $\mathbf{x}_i$ and are denoted by $\mathbf{x}_j$. For convenience, the bond vector is defined as $\mathbf{x}_{ij} = \mathbf{x}_j - \mathbf{x}_i$. The motion equation of PD is expressed in an integral form as:

$$\rho_{0i}\ddot{\mathbf{u}}_i = \int_{H_i} \left[\mathbf{T}_i\langle \mathbf{x}_{ij}\rangle - \mathbf{T}_j\langle \mathbf{x}_{ji}\rangle\right] dV_j + \mathbf{b}_i. \tag{1}$$

Here and thereafter, no summation is assumed for repeated index. Parameter $\rho = \rho(\mathbf{x}_i)$ is the mass density. $\ddot{\mathbf{u}}$ is the acceleration vector. $\mathbf{b}$ represents the body force density vector, and V_i is the volume occupied by material point i. The pair-wise force density vectors $\mathrm{T}_i\langle \mathbf{x}_{ij}\rangle$ and $\mathrm{T}_j\langle \mathbf{x}_{ji}\rangle$ represent the interactions between the material points.

$$\mathbf{T}_i\langle \mathbf{x}_{ij}\rangle = w\mathbf{P}_i\mathbf{K}_i^{-1}\mathbf{x}_{ij}. \tag{2}$$

In E q. (2), the scalar-valued function w is the weight function evaluating the influence of different neighborhood points. Usually, w is a function of bond length $|\mathbf{x}_{ij}|$. In this paper, the weight function is selected as $w = \delta/|\mathbf{x}_{ij}|$. $\mathbf{P}$ is the first Piola–Kirchhoff stress tensor expressed as:

$$\mathbf{P} = \frac{\partial \Psi}{\partial \mathbf{F}}, \tag{3}$$

with Ψ being the strain energy density function. The deformation gradient tensor $\mathbf{F}$ at the position $\mathbf{x}_i$ is expressed as:

$$\mathbf{F}_i = \left[\int_{H_i} w(|\mathbf{x}_{ij}|)\cdot\left(\mathbf{y}_{ij}\otimes\mathbf{x}_{ij}\right)dV_j\right]\mathbf{K}_i^{-1}, \tag{4}$$

where symbol $\otimes$ denotes the dyadic product of two vectors. $\mathbf{y}$ is the position vector in the current configuration. The shape tensor $\mathbf{K}$ is written as:

$$\mathbf{K}_i = \int_{H_i} w\cdot\left(\mathbf{x}_{ij}\otimes\mathbf{x}_{ij}\right)dV_j. \tag{5}$$

Besides, one may deduce or define a non-local differential operator [35] similar to Eq. (4):

$$\nabla_{\mathbf{x}}\otimes\mathbf{f}|_{\mathbf{x}_i} = \left[\int_{H_i} w(|\mathbf{x}_{ij}|)\left(\mathbf{f}_{ij}\otimes\mathbf{x}_{ij}\right)dV_j\right]\cdot\mathbf{K}_i^{-1}. \tag{6}$$

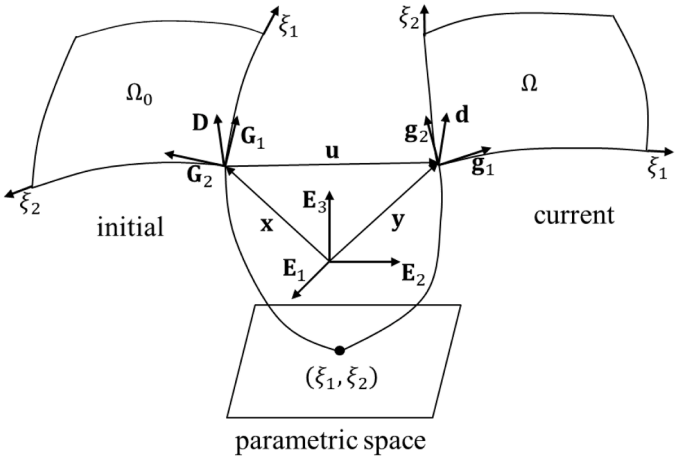

Fig. 2. Kinematic description of membrane.

3. Peridynamic formulation of membrane

3.1. Kinematics

The non-local membrane theory aims to simplify the curving horizon by approximating it into a flat surface and then applying the plane stress assumption locally [36]. The kinematic description of this theory is established based on the reference provided in [37]. The kinematic interpretation of the curved membrane is illustrated in Fig. 2. The initial and current configurations are represented by mid-surface Ω_0 and Ω respectively. The membrane is modeled with one layer of material points. Each point has three degrees of freedom.

The compact parametric space is defined as $\boldsymbol{A}\subset\mathbb{R}^2$ with boundary $\partial\boldsymbol{A}$. A point in the parametric space can be denoted by:

$$\boldsymbol{\xi} = \xi_1\mathbf{E}_1 + \xi_2\mathbf{E}_2. \tag{7}$$

The position vector of a material point in the initial configuration at a distance η from the mid-surface can be written as:

$$\mathbf{x} = \boldsymbol{\Phi}^0(\xi_1,\xi_2,\eta) = \boldsymbol{\varphi}^0 + \eta\mathbf{D}(\xi_1,\xi_2),\ (\xi_1,\xi_2)\in\boldsymbol{A} \text{ and } \eta\in\left[-\frac{h}{2},\frac{h}{2}\right], \tag{8}$$

where h is the thickness of the membrane. Vector $\mathbf{D}$ is the pseudo normal vector of the membrane in the initial configuration with $|\mathbf{D}| = 1$. The convected basis vector $\mathbf{G}$ in the initial configuration is defined as the derivatives of $\boldsymbol{\Phi}^0$ with respect to parametric coordinates [36,37]:

$$\mathbf{G}_\alpha = \boldsymbol{\varphi}^0(\xi_1,\xi_2)_{,\alpha} + \eta\mathbf{D}_{,\alpha},\ \alpha = 1,2 \text{ and } \mathbf{G}_3 = \mathbf{D}. \tag{9}$$

In this work, the appropriate ξ_α is selected to make $\mathbf{G}_1$, $\mathbf{G}_2$ and $\mathbf{G}_3$ mutually perpendicular and form an orthogonal local vector basis. Similarly, the position vector in the current configuration can be written as:

$$\mathbf{y} = \boldsymbol{\Phi}(\xi_1,\xi_2,\eta) = \boldsymbol{\varphi}(\xi_1,\xi_2) + \eta\mathbf{d}(\xi_1,\xi_2),\ (\xi_1,\xi_2)\in\boldsymbol{A} \text{ and } \eta\in\left[-\frac{h}{2},\frac{h}{2}\right], \tag{10}$$

and the corresponding convected vectors are obtained by:

$$\mathbf{g}_\alpha = \boldsymbol{\varphi}(\xi_1,\xi_2)_{,\alpha} + \eta\mathbf{d}_{,\alpha}\alpha = 1,2 \text{ and } \mathbf{g}_3 = \mathbf{d}. \tag{11}$$

Here, for membrane, neglecting the shear deformation along the thickness, $\mathbf{g}_3$ is still perpendicular to $\mathbf{g}_1$ and $\mathbf{g}_2$. That is:

$$\mathbf{g}_3 = \frac{\partial\mathbf{y}}{\partial\eta} = \frac{\mathbf{g}_1\times\mathbf{g}_2}{|\mathbf{g}_1\times\mathbf{g}_2|} = \mathbf{d}. \tag{12}$$

3.2. Deformation gradient

We can express the motion from the initial configuration to the current configuration as:

$$\mathbf{F} = \frac{\partial\mathbf{y}}{\partial\mathbf{x}} = \nabla_{\mathbf{x}}\boldsymbol{\Phi}. \tag{13}$$

This motion can be regarded as the combination of two parts, i.e., from the initial configuration $\mathbf{\Phi}^0$ to the parametric configuration, and from the parametric configuration to the current configuration $\mathbf{\Phi}$. Following the chain rule, the deformation gradient can be written as:

$$\mathbf{F} = \frac{\partial \mathbf{y}}{\partial \mathbf{x}} = \nabla_{\xi}\mathbf{\Phi} \cdot \left(\nabla_{\xi}\mathbf{\Phi}^0\right)^{-1}. \tag{14}$$

Note that

$$\nabla_{\xi}\mathbf{\Phi}^0 = \nabla_{\alpha}\mathbf{\Phi}^0 + \mathbf{D} \otimes \mathbf{E}_3 = \boldsymbol{\varphi}^0_{,\alpha} \otimes \mathbf{E}_{\alpha} + \mathbf{D} \otimes \mathbf{E}_3,\ \alpha = 1, 2 \tag{15}$$

$$\nabla_{\xi}\mathbf{\Phi} = \nabla_{\alpha}\mathbf{\Phi} + \mathbf{d} \otimes \mathbf{E}_3 = \boldsymbol{\varphi}_{,\alpha} \otimes \mathbf{E}_{\alpha} + \mathbf{d} \otimes \mathbf{E}_3,\ \alpha = 1, 2 \tag{16}$$

where

$$\nabla_{\alpha} = \frac{\partial}{\partial \xi_{\alpha}}\mathbf{E}_{\alpha}\ \alpha = 1, 2. \tag{17}$$

According to Eq. (6), the derivatives of the initial position vector on the mid-surface with respect to ξ_{α} at material point i can be expressed as:

$$\boldsymbol{\varphi}^0_{,\alpha}|_i = \left[\int_{H_i} w \cdot \left(\boldsymbol{\varphi}^0_{ij} \otimes \boldsymbol{\xi}_{ij}\right) dS_j\right] \cdot \mathbf{K}_i^{-1}, \tag{18}$$

where

$$\mathbf{K}_i = \int_{H_i} w\left(|\boldsymbol{\xi}_{ij}|\right) \cdot \left(\boldsymbol{\xi}_{ij} \otimes \boldsymbol{\xi}_{ij}\right) dS_j. \tag{19}$$

Here, note that $\boldsymbol{\varphi}^0_{,\alpha}$ is a 3-by-2 matrix and $\mathbf{K}$ is a 2-by-2 matrix. Similarly, the derivatives of the current position vector on the mid-surface with respect to ξ_{α} can be expressed as:

$$\boldsymbol{\varphi}_{,\alpha}|_i = \left[\int_{H_i} w \cdot \left(\boldsymbol{\varphi}_{ij} \otimes \boldsymbol{\xi}_{ij}\right) dS_j\right] \cdot \mathbf{K}_i^{-1}. \tag{20}$$

Then, $\nabla_{\xi}\mathbf{\Phi}^0$ can be written in a matrix form as:

$$\nabla_{\xi}\mathbf{\Phi}^0 = \begin{bmatrix} \frac{\partial \varphi^0_1}{\partial \xi_1} & \frac{\partial \varphi^0_1}{\partial \xi_2} & D_1 \\ \frac{\partial \varphi^0_2}{\partial \xi_1} & \frac{\partial \varphi^0_2}{\partial \xi_2} & D_2 \\ \frac{\partial \varphi^0_3}{\partial \xi_1} & \frac{\partial \varphi^0_3}{\partial \xi_2} & D_3 \end{bmatrix} = [\,\mathbf{G}_1 \quad \mathbf{G}_2 \quad \mathbf{D}\,], \tag{21}$$

and $\nabla_{\xi}\mathbf{\Phi}$ can be written as:

$$\nabla_{\xi}\mathbf{\Phi} = \begin{bmatrix} \frac{\partial \varphi_1}{\partial \xi_1} & \frac{\partial \varphi_1}{\partial \xi_2} & d_1 \\ \frac{\partial \varphi_2}{\partial \xi_1} & \frac{\partial \varphi_2}{\partial \xi_2} & d_2 \\ \frac{\partial \varphi_3}{\partial \xi_1} & \frac{\partial \varphi_3}{\partial \xi_2} & d_3 \end{bmatrix} = [\,\mathbf{g}_1 \quad \mathbf{g}_2 \quad \mathbf{d}\,]. \tag{22}$$

Please note that vector $\mathbf{d}$ only represents the direction and does not contain any information about the thickness stretch. Specially, if the initial configuration is flat, then$\xi_I = x_I$ and $\mathbf{G}_I = \mathbf{E}_I$. Thus $\nabla_{\xi}\mathbf{\Phi}^0$ is becomes an identity matrix. For convenience, in all following samples, the initial configuration is always flat.

3.3. Non-local balance law of linear momentum

In the work of [37], the balance laws and nonlocal governing equations for peridynamic shells were derived based on the element perspective. These equations are also applicable to PD membrane structures. The governing equation for the linear momentum of the membrane in non-local form at the mid-plane is given below:

$$\rho_0 \ddot{\varphi}_i = \int_{H_i} \left[\overline{\mathbf{T}}_i\langle \boldsymbol{\xi}_{ij}\rangle - \overline{\mathbf{T}}_j\langle \boldsymbol{\xi}_{ji}\rangle\right] dS_j + \overline{\mathbf{b}}_i, \tag{23}$$

with

$$\overline{\mathbf{b}} = \det\left(\nabla_{\xi}\mathbf{\Phi}^{0}\right)\mathbf{b}. \tag{24}$$

And $\overline{\mathbf{T}}$ is the force density vector defined on the mid-surface expressed as:

$$\overline{\mathbf{T}}_i\langle\boldsymbol{\xi}_{ij}\rangle = w\left(|\boldsymbol{\xi}_{ij}|\right)\widehat{\mathbf{P}}_i^0\mathbf{K}_i^{-1}\boldsymbol{\xi}_{ij}, \tag{25}$$

where

$$\widehat{\mathbf{P}} = \det\left(\nabla_{\xi}\mathbf{\Phi}^{0}\right)\mathbf{P}\left(\nabla_{\xi}\mathbf{\Phi}^{0}\right)^{-1}, \tag{26}$$

and

$$\widehat{\mathbf{P}}^{0} = \begin{bmatrix} \widehat{P}_{11} & \widehat{P}_{12} \\ \widehat{P}_{21} & \widehat{P}_{22} \\ \widehat{P}_{31} & \widehat{P}_{32} \end{bmatrix}. \tag{27}$$

4. Constitutive model and neural network method

4.1. Enforcement of plane stress and slight compressibility on Neo-Hookean model

In the presented study, the Neo-Hookean model, a representative constitutive hyperelastic model is taken as the example in the analysis. The strain energy density function is expressed as:

$$\Psi = \frac{\mu}{2}(\bar{I}_1 - 3) + \frac{K}{8}\left(J - J^{-1}\right)^2, \tag{28}$$

where μ is the shear modulus, $\bar{I}_1$ the normalized first invariant of right Cauchy-Green strain tensor which is written as $\bar{I}_1 = tr\mathbf{C}J^{-2/3}$, with $\mathbf{C} = \mathbf{F}^T\mathbf{F}$ and $J = \det\mathbf{F}$. Parameter K represents the bulk modulus. The slightly compressible model leads to a relatively large K compared to the shear modulus. In this article, K is set to 100 times the shear modulus. The first Piola–Kirchhoff stress tensor can be expressed as:

$$\mathbf{P} = \frac{\partial\Psi}{\partial\mathbf{F}} = \mu\left(\mathbf{F} - \frac{1}{3}tr\mathbf{C}\mathbf{F}^{-T}\right)J^{-2/3} + \frac{K}{4}\left(J^2 - J^{-2}\right)\mathbf{F}^{-T}. \tag{29}$$

The first Piola–Kirchhoff stress tensor under plane stress assumption is expressed as follows, which is explained in Ref. [19]:

$$\widetilde{\mathbf{P}} = \mu\left(\widetilde{\mathbf{F}} - C_{33}\widetilde{\mathbf{F}}^{-T}\right)C_{33}^{-1/3}\widetilde{J}^{-2/3}, \tag{30}$$

where $\widetilde{J} = \det\widetilde{\mathbf{F}}$ with $\widetilde{\mathbf{F}}$ being the in-plane deformation gradient tensor. In this article, the superscript $\sim$ denotes that the tensors exist in 2D space. C_{33} is a component of the right Cauchy-Green strain tensor $\mathbf{C}$, which can be obtained numerically through the equation:

$$\mu\left(\frac{2}{3}C_{33}^{-2/3} - \frac{1}{3}C_{33}^{-1/3}tr\widetilde{\mathbf{C}}\right)\widetilde{J}^{-2/3} + \frac{K}{4}\left(C_{33}\widetilde{J}^2 - C_{33}^{-1}\widetilde{J}^{-2}\right) = 0. \tag{31}$$

A nondimensionalized first Piola-Kirchhoff stress tensor is defined as below:

$$\widetilde{\mathbf{P}}^{*} = \widetilde{\mathbf{P}}\Big/\mu = \left(\widetilde{\mathbf{F}} - C_{33}\widetilde{\mathbf{F}}^{-T}\right)C_{33}^{-1/3}\widetilde{J}^{-2/3}, \tag{32}$$

with corresponding C_{33} calculated as:

$$\left(\frac{2}{3}C_{33}^{-2/3} - \frac{1}{3}C_{33}^{-1/3}tr\widetilde{\mathbf{C}}\right)\widetilde{J}^{-2/3} + \frac{100}{4}\left(C_{33}\widetilde{J}^2 - C_{33}^{-1}\widetilde{J}^{-2}\right) = 0. \tag{33}$$

4.2. A novel mapping to the force density vector

In the conventional NOSB PD formulation, the force density vector of a bond is determined by its deformation gradient tensor (see Eq. (2) to Eq. (4)). However, such a framework suffers from zero-energy modes, where different displacement states of a horizon can be mapped into the same deformation gradient tensor through Eq. (4). For example, in Ref. [24], when a single point movement is applied to the central point of a horizon, the deformation gradient remains unchanged and the strain energy remains the same, leading to zero-energy modes. To avoid these zero-energy modes, this work constructs a direct mapping from the bond vectors including bond stretch and rotation with some other variables to the force density vector.

First, the force density vector Eq. (2) is rewritten in a general form as:

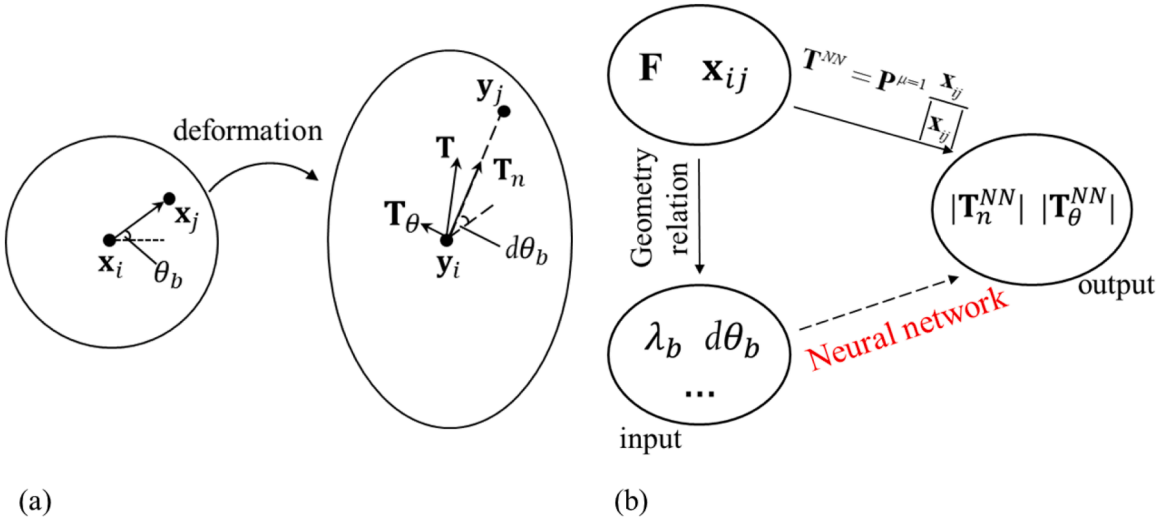

Fig. 3. Notations of bond-related quantities during deformation. (b) Illustration of the desired mapping.

$$\mathbf{T}_i\langle\mathbf{x}_{ij}\rangle = w \cdot fac_{\mathbf{K}} \cdot \mu \cdot |\mathbf{x}_{ij}| \cdot \mathbf{T}^{NN}. \tag{34}$$

where, $\mathbf{T}^{NN}$is a non-dimensionalized force vector. In this analysis, the non-dimensionalized force vector is only corresponding with the deformation gradient. The effects of other parameters on $\mathbf{T}^{NN}$are totally eliminated. Thus, which is more general, and expressed in the form:

$$\mathbf{T}^{NN} = \mathbf{T}_i^{NN}\langle\mathbf{x}_{ij}\rangle = \mathbf{P}_i^*\mathbf{x}_{ij}^* \text{ with } \mathbf{P}_i^* = \mathbf{P}_i \Big/ \mu \text{ and } \mathbf{x}_{ij}^* = \mathbf{x}_{ij} \Big/ |\mathbf{x}_{ij}|. \tag{35}$$

For a symmetric horizon, the shape tensor $\mathbf{K}$ is a diagonal matrix with identical diagonal elements. Thus, it can be simplified as a factor $fac_{\mathbf{K}}$, and expressed in a discretized form:

$$fac_{\mathbf{K}} = 2 \Big/ \left(\sum_{j\in H_i} w(|\mathbf{x}_{ij}|)\mathbf{x}_{ij,1}^2 V_j + \sum_{j\in H_i} w(|\mathbf{x}_{ij}|)\mathbf{x}_{ij,2}^2 V_j \right), \tag{36}$$

with $\mathbf{x}_{ij,1}$ and $\mathbf{x}_{ij,2}$ representing the components of the bond vector $\mathbf{x}_{ij}$.

The force density vector is decomposed into two components: one along the direction of deformed bond denoted by $\mathbf{T}_n$ and the other tangent to the deformed bond denoted by $\mathbf{T}_\theta$, as illustrated in Fig. 3 (a). It is important to note that the positive direction of $\mathbf{T}_n$ is pointing form $\mathbf{y}_i$ to $\mathbf{y}_j$, and the counter-clockwise direction is defined as the positive direction of θ and $\mathbf{T}_\theta$. Additionally, $\mathbf{T}^{NN}$ is also separated into two parts, one along the deformation direction of the bond denoted as $\mathbf{T}_n^{NN}$ and the other tangent to the bond denoted as $\mathbf{T}_\theta^{NN}$, using the same method.

The deformation gradient tensor of an incompressible material can be formed solely with principal stretches. In the 2D case, it takes the following form:

$$\widetilde{\mathbf{F}} = \begin{bmatrix} \lambda_1 & 0 \\ 0 & \lambda_2 \end{bmatrix}, \tag{37}$$

where λ_1 and λ_2 represent the in-plane principal stretches. With the information of deformation gradient $\mathbf{F}$ and a certain bond vector, the bond stretch λ_b and the bond rotation $d\theta_b$ can be obtained through the geometric relation. The bond stretch is expressed as:

$$\lambda_b = \frac{|\mathbf{y}_{ij}|}{|\mathbf{x}_{ij}|} = \frac{|\mathbf{y}_{ij}^*|}{|\mathbf{x}_{ij}^*|}, \text{ with } \mathbf{y}_{ij} = \widetilde{\mathbf{F}}_i\mathbf{x}_{ij}, \text{ and } \mathbf{y}_{ij}^* = \widetilde{\mathbf{F}}_i\mathbf{x}_{ij}^*. \tag{38}$$

The rotation angle is calculated as:

$$d\theta_b = \arcsin\left(\frac{\mathbf{x}_{ij} \times \mathbf{y}_{ij}}{|\mathbf{x}_{ij}| \cdot |\mathbf{y}_{ij}|}\right) = \arcsin\left(\frac{\mathbf{x}_{ij}^* \times \mathbf{y}_{ij}^*}{|\mathbf{x}_{ij}^*| \cdot |\mathbf{y}_{ij}^*|}\right). \tag{39}$$

In order to find the mapping from the bond-related variables to $\mathbf{T}^{NN}$, a deep neural network with λ_b, $d\theta_b$, C_{33} and $\det(\widetilde{\mathbf{F}})$ as the input, $|\mathbf{T}_n^{NN}|$ and $|\mathbf{T}_\theta^{NN}|$ as the output is constructed. The process is illustrated in Fig. 3 (b).

Algorithm 1
Pseudocode for generating training data

for various λ_1 and λ_2
build the in-plane deformation gradient tensor $\widetilde{\mathbf{F}}$ by Eq. (37)
for various bond orientations $\theta_b \in (0,2\pi]$
The normalized bond vector is $\mathbf{x}_{ij}^{n} = (\cos\theta_b, \sin\theta_b)^{\mathrm{T}}$
calculate C_{33} by Eq. (33)
calculate $\widetilde{\mathbf{P}}^{*}$ by Eq. (32)
calculate force density vector $\mathbf{T}^{NN}$ by Eq. (35)
decompose $\mathbf{T}^{NN}$ into $\mathbf{T}_n^{NN}$ and $\mathbf{T}_\theta^{NN}$
calculate bond stretch λ_b by Eq. (38) and rotation angle $d\theta_b$ by Eq. (39)
write input data: λ_b, $d\theta_b$, C_{33}, det$\mathbf{F}$
write corresponding output data: $|\mathbf{T}_n^{NN}|$, $|\mathbf{T}_\theta^{NN}|$
end
end

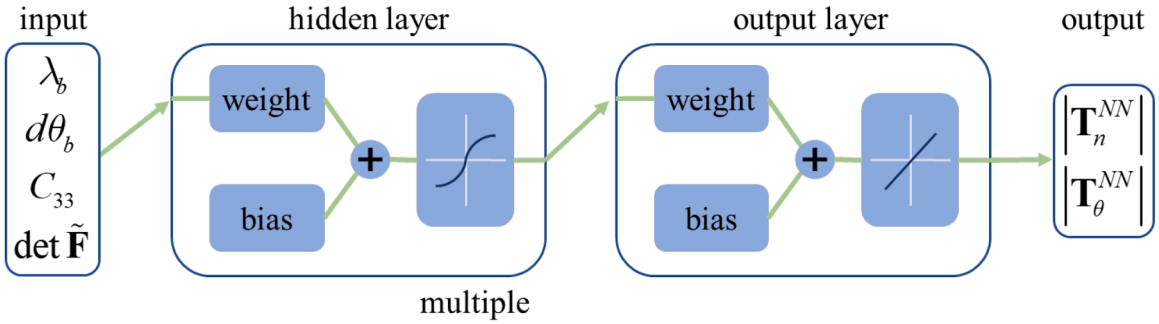

Fig. 4. Illustration of the designed NN.

4.3. Generation of training data

The following is the pseudocode for generating training data, as outlined in Algorithm 1. The neural network is set with four neurons as the input and two neurons as the output, as is shown in Fig. 4. The principle stretches λ_1 and λ_2 of the deformation gradient are set to cover common deformation states of rubber-like materials in plane stress case, with values ranging from 0.8 to 4.0, respectively. The normalized bond vector $\mathbf{x}_{ij}/|\mathbf{x}_{ij}|$ is set with various orientations. Note that the tensors in the algorithm are all in 2D case for plane stress assumption. By considering a wide deformation state and bond vector, around 10000 samples are generated in the training data. The training process is performed through the neural network fitting tool on Matlab. 70 % of the dataset is used for training the model. The proportions for validation and prediction are both 15 %. There is no noise in the process of generating training data. Thus, a high accuracy of around 99 % is obtained by the trained NN.

5. Implementation of the proposed NN NOSB PD

5.1. Apply the NN method to the local deformation state

In order to support the plane stress hypothesis, the interactions between the material points are evaluated in the local coordinate system. To achieve this, an orthonormal tensor $\mathbf{Q}$ is applied to the horizon in the current configuration, to rotate vector $\mathbf{g}_1$, $\mathbf{g}_2$ and $\mathbf{d}$ approximately along the direction of $\mathbf{E}_1$, $\mathbf{E}_2$ and $\mathbf{E}_3$, respectively. It's worth noting that in the case of incompressible material, $\mathbf{g}_1$ and $\mathbf{g}_2$ are almost orthogonal to each other during the deformation. Therefore, the deformation gradient in the local system can be expressed as:

$$\mathbf{F}^{l} = \mathbf{Q}\mathbf{F}. \tag{40}$$

Then, the 2-by-2 deformation gradient tensor for the local plane stress assumption is formed as:

$$\widetilde{\mathbf{F}}^{l} = \begin{bmatrix} F_{11}^{l} & F_{12}^{l} \\ F_{21}^{l} & F_{22}^{l} \end{bmatrix}. \tag{41}$$

Instead of using the conventional NOSB PD formulation to obtain the local force density vector through Eq. (2), the proposed NN method is used. The NN method requires the calculation of four input variables. λ_b is calculated using Eq. (38). $d\theta_b$ is obtained as

Algorithm 2
Pseudocode for PD implementation

Preparation: Discrete the model and create arrays to store the initial position vector **x**, deformed position vector **y**, and displacement vector **u**.
  Search and store the neighborhood points for each material point.
  Build an input matrix in dimension *n_total_bond*×4 (λ_b, $d\theta$, C_{33}, det**F**), and an output matrix in dimension *n_total_bond*×2 ($|\mathrm{T}_n^{NN}|$, $|\mathrm{T}_\theta^{NN}|$).
  for *tt* = 1: *max_time_step*
   apply the boundary conditions
   calculate $C_{33(i)}$ and det$\mathbf{F}_i$ for each node
   for *i* = 1: *total_node*
   calculate the global deformation gradient (Eq. 14)
   form the rotation matrix **Q** and calculate the local deformation gradient
   for *j* = 1: *n_neighbor*
   calculate λ_b, $d\theta_b$(Eq. 42) for the bond
   write the λ_b, $d\theta$, C_{33} and det**F** to the certain row of input matrix
   end
   end
   use the neural network to obtain T_n^{NN}
   form the local force density vector $\mathbf{T}^l$ of each bond
   calculate the global force density vector (Eq. 43)
   assemble the force density to each material point
   update the position of material points by the kinetic equation
  end

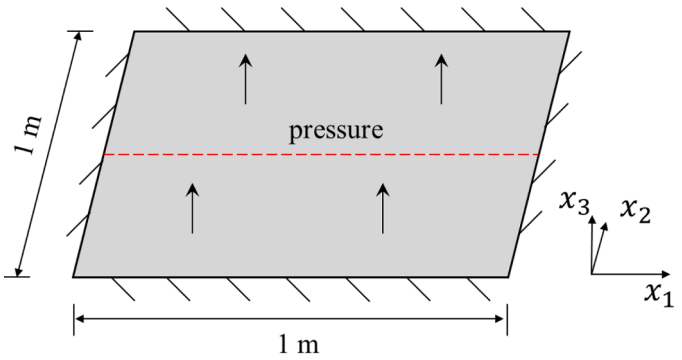

Fig. 5. Geometry and boundary conditions of a Neo-Hookean membrane under pressure.

$$d\theta_b = \arcsin\left(\frac{\mathbf{x}_{ij} \times \mathbf{y}_{ij}^l}{|\mathbf{x}_{ij}| \cdot |\mathbf{y}_{ij}^l|}\right), \text{ with } \mathbf{y}_{ij}^l = \mathbf{Q}\mathbf{y}_{ij}. \tag{42}$$

C_{33} and $\det(\widetilde{\mathbf{F}})$ are calculated based on $\widetilde{\mathbf{F}}^l$. Thus, the local force density vector $\mathbf{T}^l$ can be obtained through the trained NN model and then transformed into the global system as:

$$\mathbf{T} = \mathbf{Q}^T\mathbf{T}^l. \tag{43}$$

5.2. Framework of the program

In the PD implementation, the considered domain is discretized uniformly into material points. The quasi-static solutions are achieved by adding a numerical damping term c in the equation of motion. Thus, Eq. (1) is rewritten as:

$$\rho_i\ddot{\mathbf{x}}_i = \int_{H_i}\left[\mathbf{T}_i\langle\mathbf{x}_{ij}\rangle - \mathbf{T}_j\langle\mathbf{x}_{ji}\rangle\right]dV_j + \mathrm{b}_i - c\dot{\mathbf{x}}_i. \tag{44}$$

To solve the equation of motion, the explicit central difference method is used. In order to optimize efficiency, an input matrix is created to store the input information for the NN of each bond. Instead of calling the trained NN model for each bond independently, the input matrix for all the bonds is delivered to the constructed trained NN model at every time step to save time. For a detailed understanding of the implementation process, please refer to Algorithm 2.

6. Numerical examples

In this work, uniform discretization is used for all numerical examples. The horizon radius is consistently set at $\delta = 3.15\,dx$. Unless specified otherwise, the Neo-Hookean material parameters are set as mass density $\rho = 1000.0$ kg/m^3, shear modulus $\mu = 1.0$ kPa and

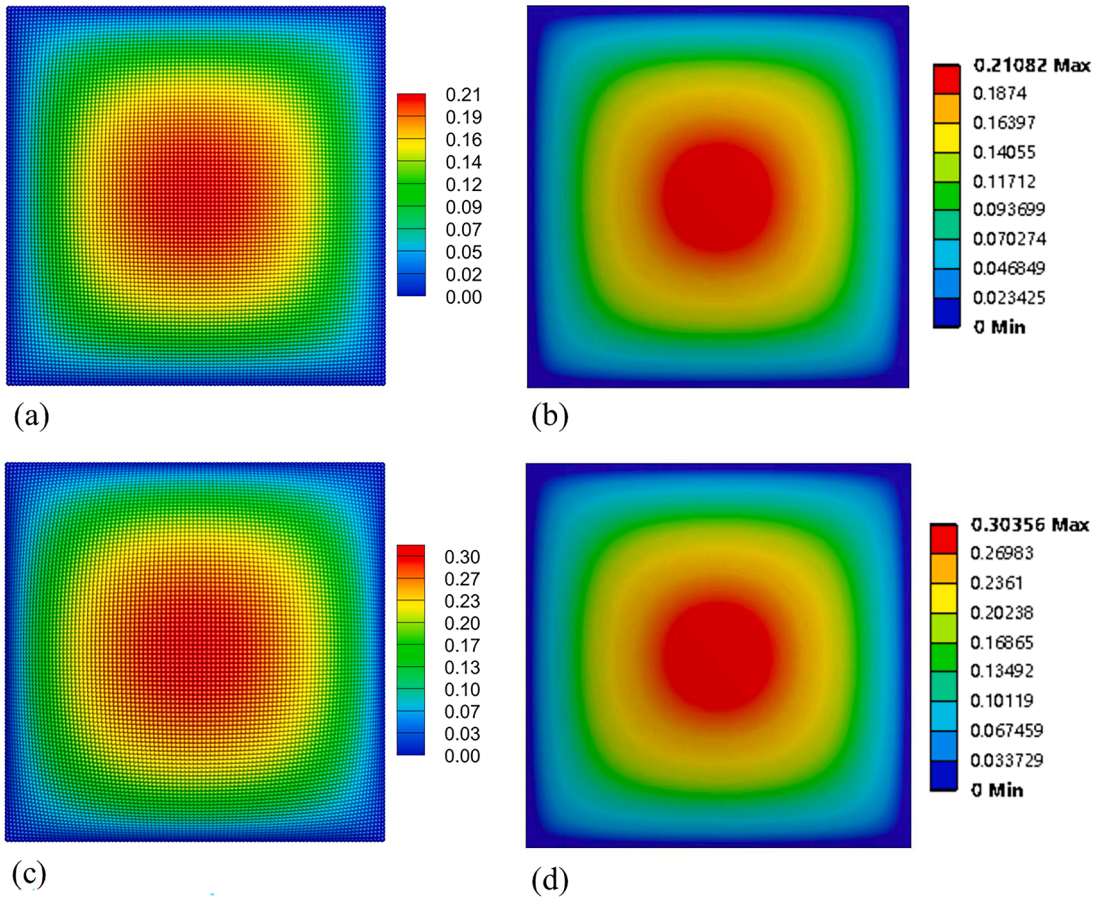

Fig. 6. Displacement contours of the membrane under pressure. (a) PD result with $p = 10$ Pa. (b) FEM result with $p = 10$ Pa. (c) PD result with $p = 20$ Pa. (d) FEM result with $p = 20$ Pa.

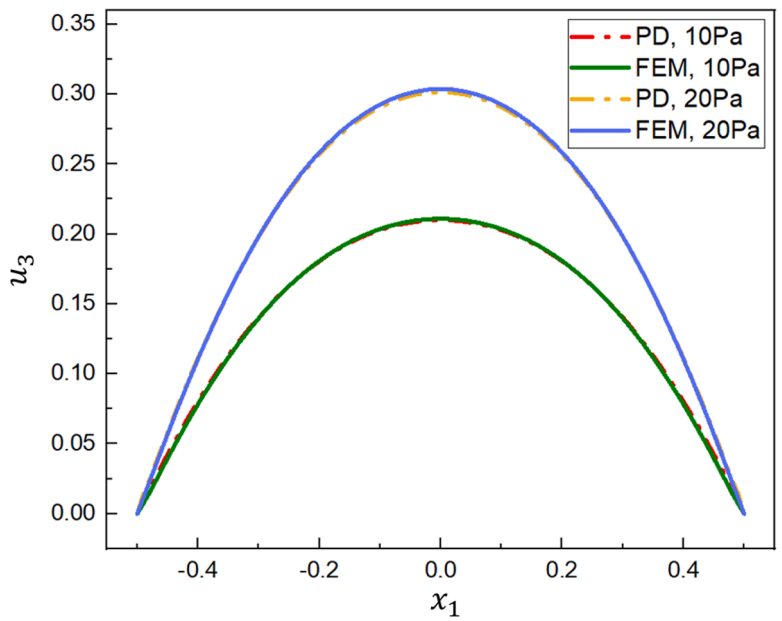

Fig. 7. Comparisons of the displacement along the center line.

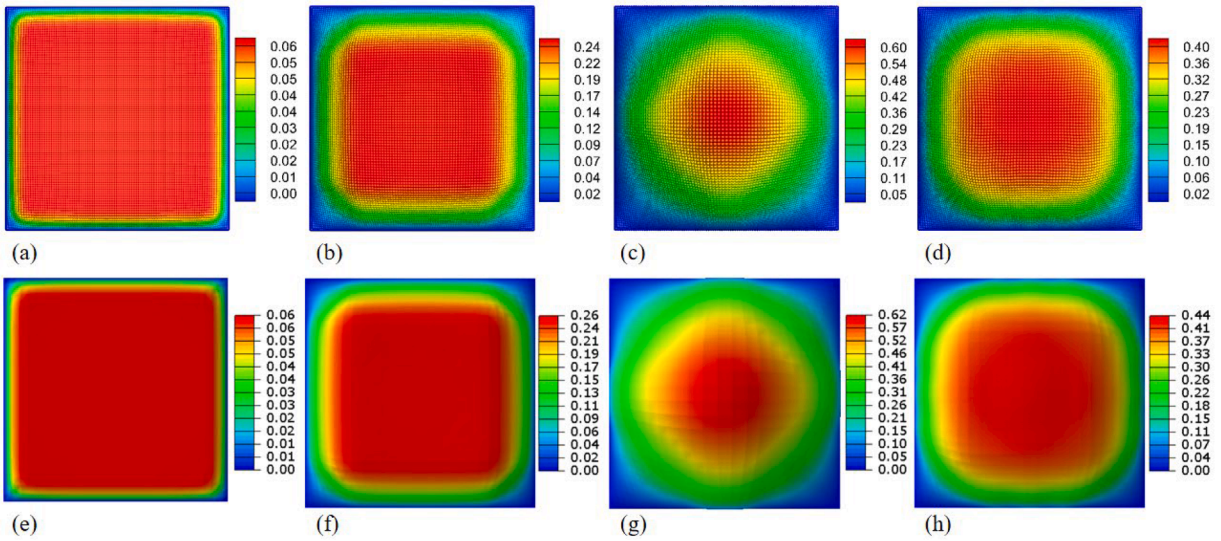

Fig. 8. Contours of u_3 at $t = 0.25$s, 0.50s, 0.75s, 1.00s, respectively. The first row and the second rows are the predictions from present PD and FEM, respectively.

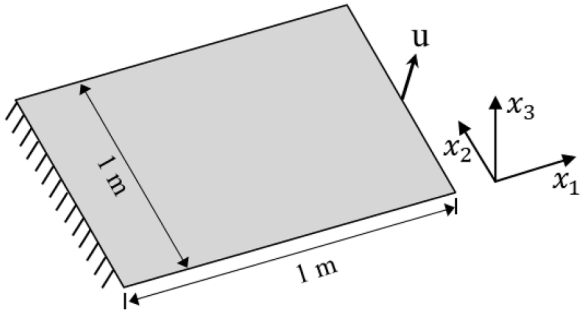

Fig. 9. Illustration of the membrane under out-of-plane loading.

bulk modulus $K = 100.0$ kPa, unless specified otherwise.

6.1. Membrane under normal pressure

Fig. 5 shows that the Neo-Hookean sheet has a dimension of 1 m × 1 m × 0.01 m, with all four edges fixed. Pressure is applied normally to its surface. The spatial discretization size for the PD model is 0.01 m. Simulations are performed under two different pressures: $p = 10$ Pa and $p = 20$ Pa. The contours of the displacement component u_3 on the current configuration are shown in Fig. 6. The first and second rows are the results with pressures of 10 Pa and 20 Pa, respectively. The left column displays the quasi-static result predicted by the proposed NN PD, while the right column shows the FEM result performed on ANSYS. The results of u_3 on the center line of the membrane (the red dashed line in Fig. 5) are plotted in Fig. 7. The predicted values from PD and FEM are very close, which demonstrates the accuracy of the proposed method.

Meanwhile, the dynamic response under pressure of 20 Pa is also simulated and compared with FEM predictions. The finite element analysis is performed on ABAQUS. The Rayleigh damping is applied. The coefficient associated with the mass matrix term is set 0.1. The pressure is applied at $t = 0$s. Explicit dynamic analysis is performed till $t = 1$s. The contours of u_3 are presented in Fig. 8, at $t =$ 0.25s, 0.50s, 0.75s, 1.00s, respectively. The FEM predictions and PD predictions are very close. In terms of the maximum value of u_3, the deviations between the PD predicted values and FEM predicted values are all within 5 %.

6.2. Out-of-plane loading on a membrane

As shown in Fig. 9, the membrane has dimensions of 1 m × 1 m × 0.01 m and the left edge is fixed. Displacements **u** are applied to several material points within 0.04 m distance from the center point of the right edge. The displacement has components along the x_1 and x_3 direction, which is defined as: $u_1 = 0.025t$ and $u_3 = 0.05t$, respectively, where t is time in seconds. After 2 seconds, the applied

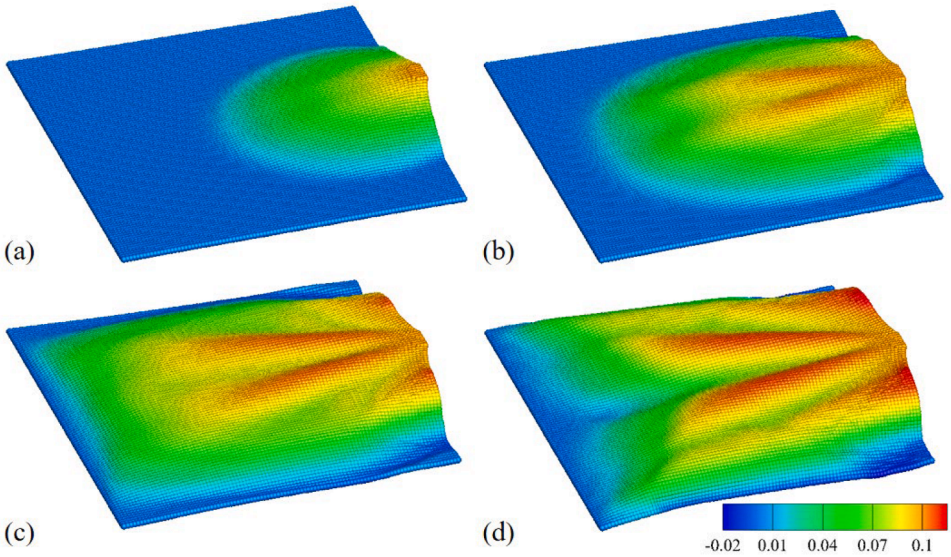

Fig. 10. Contours of displacement along u_3 direction at $t =$ (a) 1.5s, (b) 2.5s, (c) 3.5s, (d) 4.5s.

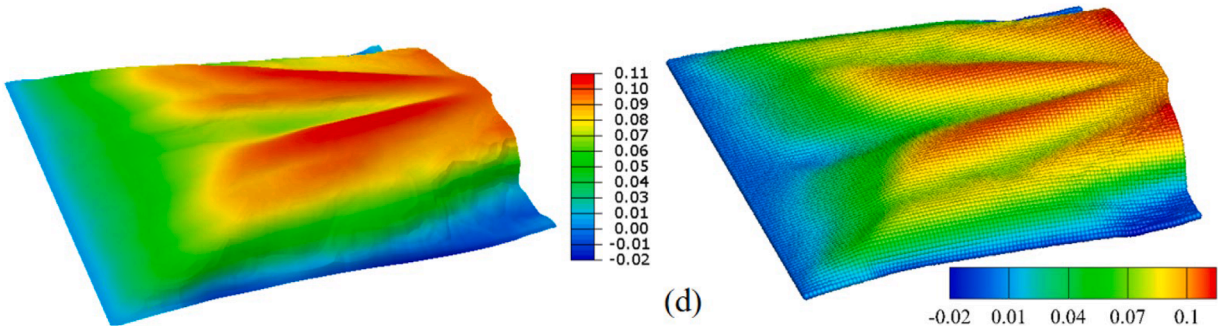

Fig. 11. Contours of displacement along u_3 direction at $t = 4.5$s, (a) ABAQUS, (b) present PD.

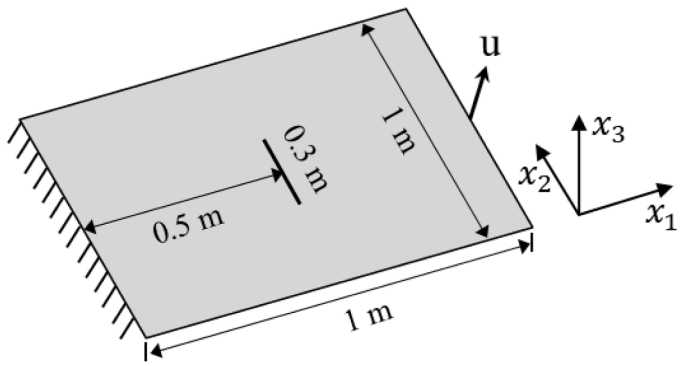

Fig. 12. Illustration of the membrane under out-of-plane loading with a precut.

displacement is fixed at a constant value of $u_1 = 0.05$m and $u_3 = 0.1$m. The spatial discretization size for the PD model is 0.01 m. Some deformation contours are presented in Fig. 10, at $t = 1.5$s, 2.5s, 3.5s and 4.5s, respectively.

In this example, a rectangular membrane is fixed along its left side while the other sides are free. A segment of the membrane is pulled upward (out of the plane) with constant velocity. Stress concentrations are created at the ends of the lifted segment. Over time, these stress concentrations lead to a deformation that spreads in a wide range, with two main branches.

This numerical sample is also conducted using ABAQUS. An explicit dynamic analysis is carried out up to $t = 4.5$s. The comparison

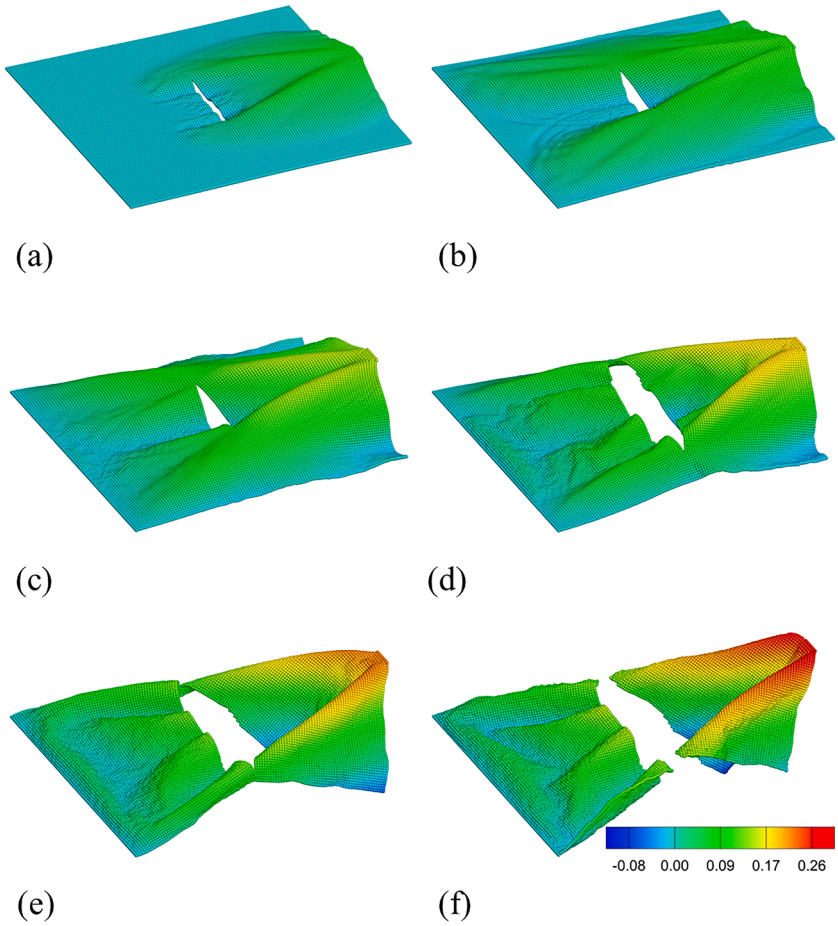

Fig. 13. Contours of displacement along u_3 direction at t = (a) 3.0s, (b) 4.5s, (c) 6.0s, (d) 7.5s, (e) 9.0s, (d) 10.5s.

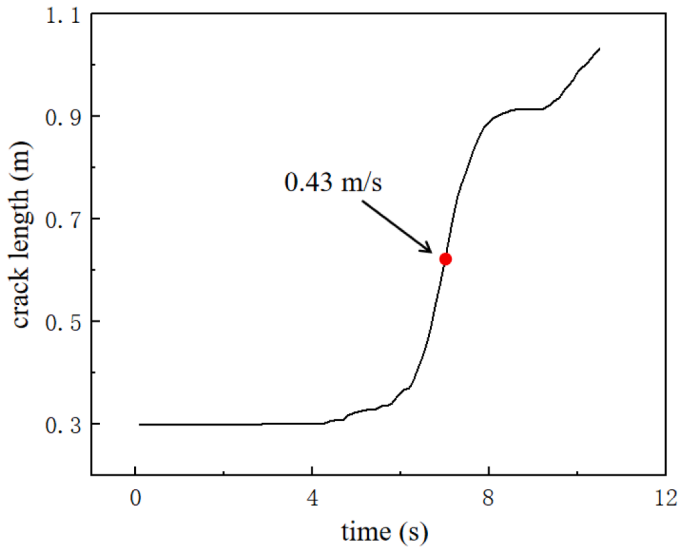

Fig. 14. Crack length with respect to time.

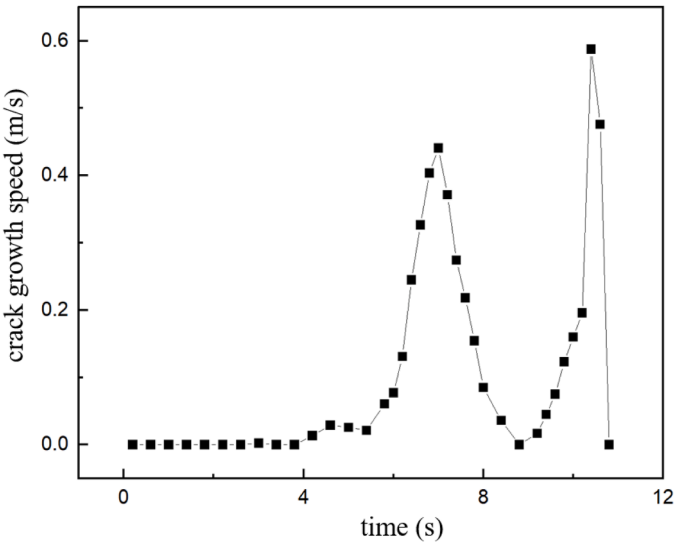

Fig. 15. Crack growth speed with respect to time.

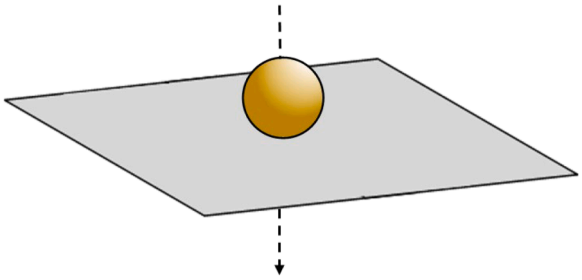

Fig. 16. Illustration of a ball penetrating through a membrane.

between the results of present PD and FEM is shown in Fig. 11, displaying the contours of u_3 at t = 4.5s. It can be observed that the results are in agreement.

6.3. Out-of-plane loading on a membrane with a precut

As shown in Fig. 12, the geometry of the example is the same as that in Section 6.2, except for a precut in the center. A displacement with components along the x_1 and x_3 direction is applied at several points around the center point of the right edge, until the membrane is separated into 2 parts. The applied displacement is defined as: $u_1 = 0.0125t$ and $u_3 = 0.025t$. The domain is discretized into 14400 material points.

The PD model is used to describe failure by removing the interaction forces between paired material points. In the case of Neo-Hookean material, failure occurs when the bond stretch λ_b exceeds the critical value λ_c, which is known as the effective stretch criterion [38]. For this example, λ_c is set to 1.3. To record the failure, the force density vector is modified using a history-dependent function γ, which is expressed as:

$$\gamma(\lambda_b, t) = \begin{cases} 1, \text{if} \lambda_b < \lambda_c \text{forall} 0 \le t' \le t \\ 0, \text{otherwise} \end{cases}. \tag{45}$$

Fig. 13 illustrates the evolution of a slit turning into a dynamic crack at six different stages. In view (a), the slit has not yet commenced growing and wrinkles can be seen along the edges of the slit. These wrinkles arise spontaneously because the edges are free along the normal to the slit and tend to develop compressive strains parallel to the slit. Small initial displacements that vary sinusoidal throughout the numerical model "seed" these wrinkles. In the subsequent views of the figure. the crack is propagating and wrinkles appear in the wake of the crack. Fig. 14 and Fig. 15 show the crack length and the crack growth speed with respect to time, respectively.

6.4. Penetration of a ball through a membrane

As shown in Fig. 16, the membrane is a 1 m × 1 m × 0.01 m dimension structure with four fixed edges. A rigid ball with a diameter

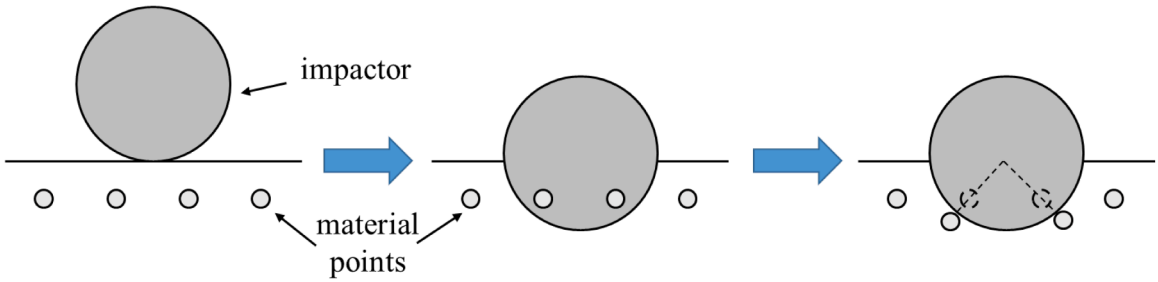

Fig. 17. Schematic of relocation of the contacted nodes.

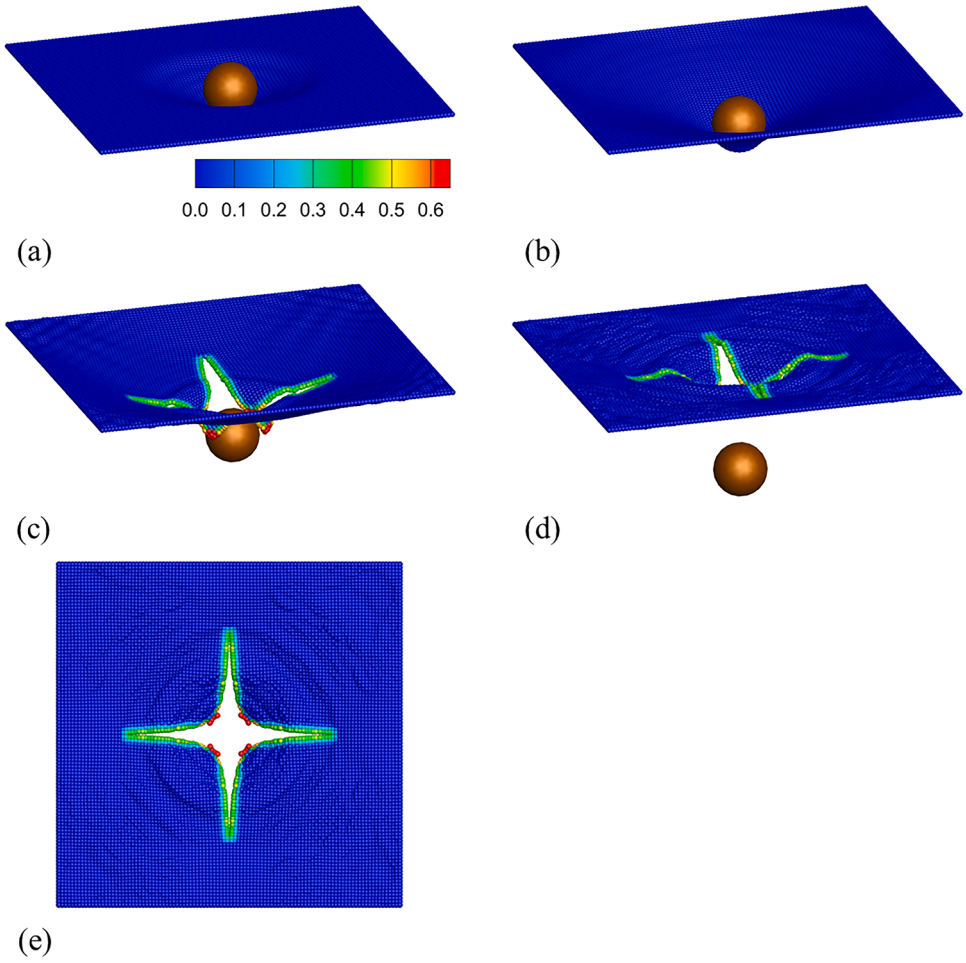

Fig. 18. Contours of damage at $t =$ (a) 1.0s, (b) 2.0s, (c) 3.0s, (d) 4.0s. (e) The top view of the cracked membrane at $t = 4.0$s.

of 0.15 m moves downwards and penetrates the membrane. The velocity of the ball is 0.1 m/s. At $t = 0$s, the ball makes contact with the membrane. The friction between the ball and membrane is neglected. The membrane is discretized into 10000 material points. The critical stretch λ_c is set at 1.3.

As the moving of the ball, if the material points of the membrane in contact with the ball, they will move to the nearest distance to the impact surface. The treatment of the contact process is depicted in Fig. 17. The same schematic of impact is also explained in Ref. [39]. The damage incurred by the material points is defined as:

$$dmg_i = 1 - \frac{\int_{H_i} \gamma(\lambda_b, t) dV_j}{\int_{H_i} dV_j}. \tag{46}$$

Fig. 18 illustrates the damage patterns of various processes in the simulation. The first four patterns are at $t = 1.0$s, 2.0s, 3.0s and 4.0s, correspondingly. To view the crack clearly, the top view of the cracked membrane is provided in Fig. 17 (e) at $t = 4.0$s.

7. Conclusions

In this paper, a new algorithm for modeling the large deformation and failure behavior of hyperelastic membranes is proposed. It introduces a non-local membrane theory based on the assumption of plane stress. This leads to the simulation of the membrane structure using a single layer of material points, simplifying implementation, improving efficiency, and avoiding volume locking. The constitutive function of rubber-like materials can be directly introduced in the governing equation of NOSB PD by the first Piola-Kirchhoff stress. Thus, it is generally applicable to any constitutive law of hyperelastic materials. A deep neural network technique is used to achieve a novel mapping between the deformation state and the force density vector in the PD framework. This new mapping eliminates the numerical instability and oscillations caused by using the traditional NOSB PD to solve the force density vectors, avoiding calculation of the deformation gradient of each bond to improve great efficiency. Most important is the developed method can accurately and efficiently model the large deformation, out-of-plane tearing, wrinkles as well as fracture of hyperelastic membranes. The accuracy of the proposed method is validated through comparisons with FEM results and experiment data.

CRediT authorship contribution statement

Yang Yang: Writing – review & editing, Writing – original draft, Supervision, Methodology. **Yujie Chen:** Writing – original draft, Software, Data curation. **Yijun Liu:** Writing – review & editing, Supervision.

Declaration of competing interest

The authors declare that they have no known competing financial interests or personal relationships that could have appeared to influence the work reported in this paper.

Data availability

Data will be made available on request.

Acknowledgments

The authors would like to thank the financial support from National Natural Science Foundation of China (Project Nos. 12272160 and 12372198) and the Shenzhen National Science Foundation (Project No. 20231129213819001).

Supplementary materials

Supplementary material associated with this article can be found, in the online version, at doi:10.1016/j.cma.2024.117239.

References

[1] J.P. Gong, Y. Katsuyama, T. Kurokawa, Y. Osada, Double-network hydrogels with extremely high mechanical strength, Adv. Mater. 15 (2003) 1155–1158.
[2] J.Y. Sun, X. Zhao, W.R.K. Illeperuma, O. Chaudhuri, K.H. Oh, D.J. Mooney, J.J. Vlassak, Z. Suo, Highly stretchable and tough hydrogels, Nature 489 (2012) 133–136.
[3] N.A. Peppas, J.Z. Hilt, A. Khademhosseini, R. Langer, Hydrogels in biology and medicine: from molecular principles to bionanotechnology, Adv. Mater. 18 (2006) 1345–1360.
[4] C. Yang, Z. Suo, Hydrogel ionotronics, Nature Rev. Mater. 3 (2018) 125–142.
[5] S.A. Silling, Reformulation of elasticity theory for discontinuities and long-range forces, J. Mech. Phys. Solids. 48 (2000) 175–209.
[6] H. Wang, L. Wu, J. Guo, C. Yu, Y. Li, J. Wang, Z. Liu, Numerical analysis on failure of sheet metals with non-ordinary state-based peridynamics, Eng. Fract. Mech. 292 (2023).
[7] Y. Jafaraghaei, T. Yu, T.Q. Bui, Peridynamics simulation of impact failure in glass plates, Theor. Appl. Fracture Mech. 121 (2022).
[8] Y.D. Ha, J. Lee, J.-W. Hong, Fracturing patterns of rock-like materials in compression captured with peridynamics, Eng. Fract. Mech. 144 (2015) 176–193.
[9] S.A. Silling, F. Bobaru, Peridynamic modeling of membranes and fibers, Int. J. Non. Linear. Mech. 40 (2005) 395–409.
[10] D.J. Bang, E. Madenci, Peridynamic modeling of hyperelastic membrane deformation, J. Eng. Mater. Technol. 139 (2017).
[11] H. Li, Y.G. Zheng, Y.X. Zhang, H.F. Ye, H.W. Zhang, Large deformation and wrinkling analyses of bimodular structures and membranes based on a peridynamic computational framework, Acta Mechanica Sinica 35 (2019) 1226–1240.
[12] B.B. Yin, W.K. Sun, Y. Zhang, K.M. Liew, Modeling via peridynamics for large deformation and progressive fracture of hyperelastic materials, Comput. Methods Appl. Mech. Eng. 403 (2023).
[13] D. Huang, G. Lu, P. Qiao, An improved peridynamic approach for quasi-static elastic deformation and brittle fracture analysis, Int. J. Mech. Sci. 94-95 (2015) 111–122.
[14] N.Rossi Cabral, M.A. Invaldi, R. Barrios D'Ambra, I. Iturrioz, An alternative bilinear peridynamic model to simulate the damage process in quasi-brittle materials, Eng. Fract. Mech. 216 (2019).

[15] Y. Liu, L. Liu, H. Mei, Q. Liu, X. Lai, A modified rate-dependent peridynamic model with rotation effect for dynamic mechanical behavior of ceramic materials, Comput. Methods Appl. Mech. Eng. 388 (2022).
[16] X. Zhang, J. Ding, Y. Zhang, A rate-dependent peridynamic model of reinforced concrete subjected to explosive loading, Eng. Fract. Mech. 292 (2023).
[17] S.A. Silling, M. Epton, O. Weckner, J. Xu, E. Askari, Peridynamic states and constitutive modeling, J. Elastic. 88 (2007) 151–184.
[18] M.S. Breitenfeld, P.H. Geubelle, O. Weckner, S.A. Silling, Non-ordinary state-based peridynamic analysis of stationary crack problems, Comput. Methods Appl. Mech. Eng. 272 (2014) 233–250.
[19] D. Behera, P. Roy, E. Madenci, Peridynamic correspondence model for finite elastic deformation and rupture in Neo-Hookean materials, Int. J. Non. Linear. Mech. 126 (2020).
[20] P. Roy, D. Behera, E. Madenci, Peridynamic simulation of finite elastic deformation and rupture in polymers, Eng. Fract. Mech. 236 (2020).
[21] S.O.M. Ozdemir, E. Oterkus, I. Amin, A. EI-Aassar, H. Shawky, Fracture simulation of viscoelastic membranes by ordinary state-based peridynamics, Procedia Struct. Integr. 41 (2022) 333–342.
[22] Y. Chen, Y. Yang, Y. Liu, Large deformation and crack propagation analyses of hydrogel by peridynamics, Eng. Fract. Mech. 284 (2023) 109261.
[23] Y. Chen, Y. Yang, Y.J. Liu, Fatigue crack growth analysis of hydrogel by using peridynamics, Int. J. Fract. 244 (2023) 113–123.
[24] A. Yaghoobi, M.G. Chorzepa, Higher-order approximation to suppress the zero-energy mode in non-ordinary state-based peridynamics, Comput. Struct. 188 (2017) 63–79.
[25] X. Gu, Q. Zhang, E. Madenci, X. Xia, Possible causes of numerical oscillations in non-ordinary state-based peridynamics and a bond-associated higher-order stabilized model, Comput. Methods Appl. Mech. Eng. 357 (2019) 112592.
[26] H. Chen, Bond-associated deformation gradients for peridynamic correspondence model, Mech. Res. Commun. 90 (2018) 34–41.
[27] H. Chen, B.W. Spencer, Peridynamic bond-associated correspondence model: Stability and convergence properties, Int. J. Numer. Methods Eng. 117 (2018) 713–727.
[28] M. Zaccariotto, T. Mudric, D. Tomasi, A. Shojaei, U. Galvanetto, Coupling of FEM meshes with Peridynamic grids, Comput. Methods Appl. Mech. Eng. 330 (2018) 471–497.
[29] Q. Liu, X.J. Xin, J. Ma, Adaptive coupling peridynamic least-square minimization with finite element method for fracture analysis, Int. J. Fract. 240 (2022) 119–141.
[30] Y. Yang, Y. Liu, Modeling of cracks in two-dimensional elastic bodies by coupling the boundary element method with peridynamics, Int. J. Solids. Struct. 217-218 (2021) 74–89.
[31] Y. Yang, Y. Liu, Analysis of dynamic crack propagation in two-dimensional elastic bodies by coupling the boundary element method and the bond-based peridynamics, Comput. Methods Appl. Mech. Eng. 399 (2022).
[32] D. Bishara, S. Li, A machine-learning aided multiscale homogenization model for crystal plasticity: application for face-centered cubic single crystals, Comput. Mech. 72 (2023) 77–93.
[33] C. Tamur, S. Li, D. Zeng, Artificial neural networks for predicting mechanical properties of crystalline polyamide12 via molecular dynamics simulations, Polymers. (Basel) 15 (21) (2023) 4254.
[34] Y. Chen, Y. Yang, Y. Liu, A neural network peridynamic method for modeling rubber-like materials, Int. J. Mech. Sci. 273 (2024) 109234.
[35] Q. Zhang, E. Madenci, A. Barut, M. Dorduncu, Peridynamic differential operator for numerical analysis, 2019.
[36] S. Li, A.M. Zhang, Y. Peng, J. Yan, A peridynamic Reissner-Mindlin shell theory, Int. J. Numer. Methods Eng. 122 (2020) 122–147.
[37] S. Li, X. Lai, L. Liu, Peridynamic modeling of brittle fracture in Mindlin-Reissner shell theory, Comput. Model. Eng. Sci. 131 (2022) 715–746.
[38] M.R. Ayatollahi, M. Heydari-Meybodi, M. Dehghany, F. Berto, A new criterion for rupture assessment of rubber-like materials under Mode-I crack loading: the effective stretch criterion, Adv. Eng. Mater. 18 (2016) 1364–1370.
[39] E. Madenci, E. Oterkus, Peridynamic theory and its applications, 2014.